Article

Integration of high strength, flexibility, and room-temperature plasticity in ceramic nanofibers

Siyu Qiang[1], Fan Wu[2], Hualei Liu[2], Sijuan Zeng[1], Shuyu Liu[3], Jin Dai[1], Xiaohua Zhang[3], Jianyong Yu[3], Yi-Tao Liu [1,3] ✉ & Bin Ding [1,2,3] ✉

The developing cutting-edge technologies involving extreme mechanical environments, such as high-frequency vibrations, mechanical shocks, or repeated twisting, require ceramic components to integrate high strength, large bending strain, and even plastic deformation, which is difficult in conventional ceramic materials. The emergence of ceramic nanofibers (CNFs) offers potential solutions; unfortunately, this desirable integration of mechanical properties in CNFs remains unrealized to date, due to challenges in precisely modulating microstructures, reducing cross-scale defects, and overcoming inherent contradictions between mechanical attributes (particularly, high strength and large deformation are often mutually exclusive). Here, we report a nucleation regulation strategy for crystalline/amorphous dual-phase CNFs, achieving an extraordinary integration of high strength, superior flexibility, and room-temperature plasticity. This advancement stems from the optimized dual-phase structure featuring reduced nanocrystal aggregation, increased internal interfaces, and the elimination of fiber defects, thus fully activating the synergistic advantages and multiple deformation mechanisms of dual-phase configurations. Using TiO_2, which is typically characterized by brittleness and low strength, as the proof-of-concept model, in-situ single-nanofiber mechanical tests demonstrate excellent flexibility, strength (~1.06 GPa), strain limit (~8.44%), and room-temperature plastic deformation. These findings would provide valuable insights into the mechanical design of ceramic materials, paving the way for CNFs in extreme applications and their widespread industrialization.

Ceramics have been indispensable in human society, yet their inherent brittleness and limited deformability severely constrain their applications in cutting-edge technologies[1,2]. For instance, aerospace thermal insulation should withstand mechanical shocks and high-frequency vibrations, while wearable devices need to endure repeated twisting. These scenarios require ceramic components to integrate high strength, large bending strain, and even plastic deformation, which is difficult in conventional ceramic materials[3,4]. The advent of one-dimensional (1D) ceramic nanofibers (CNFs) has brought a paradigm shift in the mechanical design of ceramic materials[5,6]. These bendable 1D CNFs can be strategically assembled into two-dimensional (2D) flexible membranes, three-dimensional (3D) compressible aerogels

[1]State Key Laboratory for Modification of Chemical Fibers and Polymer Materials, College of Textiles, Donghua University, Shanghai 201620, China. [2]School of Materials Science and Engineering, Shanghai University of Engineering Science, Shanghai 201620, China. [3]Innovation Center for Textile Science and Technology, Donghua University, Shanghai 200051, China. ✉e-mail: liu-yt03@dhu.edu.cn; binding@dhu.edu.cn

and stretchable sponges, enabling breakthroughs in various fields[7–11]. Targeting extreme applications and widespread industrialization, improving the comprehensive mechanical properties of CNFs is urgent and yet significantly challenging[12]. Current studies primarily focus on architectural optimizations of CNF aggregates for improving mechanics, such as cellular geometry engineering, cross-linking reinforcements, and fiber-interlocked strategies[13–15]. Despite these progress, optimizing the mechanics of single CNFs remains inescapable, as they fundamentally determine the macroscopic mechanical behavior of monolithic materials[4,5]. From an in-depth perspective, tensile strength, axial strain limit, and flexibility are probably the most crucial mechanical attributes for individual CNFs, since they collectively affect the capabilities of these structural units to absorb energy and transfer loads, thereby determining whether the macroscopic aggregates can effectively prevent stress concentrations and maintain structural stability[16,17]. Similar to the "Buckets effect", any "shortest plank" in these mechanical attributes could trigger catastrophic structural collapse in macroscopic materials under complicated stress environments.

Efforts devoted to strengthen CNFs have achieved considerable advances[18]. For example, the fine-grain strengthening effect, as described by the Hall-Petch relation, suggests that increasing grain boundaries would impede dislocation motions to enhance strength[19]. Alternatively, heterogeneous-atom doping strategies can reduce grain size and induce lattice distortions for dislocation pinning[12]. Another promising approach is amorphization, characterized by tight and strong chemical bonding within the disordered atomic arrangement[20]. However, neither hindering dislocations nor enhancing chemical bonding, can simultaneously enhance the strength and deformability of CNFs, revealing a fundamental contradiction: high strength and large strain limits are often mutually exclusive in ceramic materials[1]. Due to the high aspect ratio and sub-micron dimensions, CNFs can exhibit flexibility by accumulating minor bending deformations[12]. In comparison, facilitating tensile deformability in CNFs is much more difficult, especially for the realization of plastic behavior[21]. Recent studies indicate that room-temperature (RT) plasticity in ceramics is closely associated to crystal defects, such as high-density dislocations and stacking faults in Al_2O_3 and TiO_2, which activates slip systems at room temperature, enabling compressive plastic deformation in micropillar models[22,23]. Unfortunately, this innovative concept is less suitable to CNFs that emphasize tensile and flexural properties, as cross-scale defects (spanning morphological, microporous, and crystalline levels) are prone to stress concentrations under load, potentially weakening their tensile strength and flexibility[12]. These inherent mechanical contradictions in CNFs severely hinder the simultaneous optimization of their comprehensive mechanical properties.

Recently, crystalline/amorphous dual-phase (DP) ceramic materials comprising a disordered matrix and embedded nanograins are presented, revealing impressive mechanical mechanisms: nanocrystal domains stabilize the disordered regions to prevent structural failures, while the amorphous matrix acts as a soft boundary to dissipate stress[4,6,24,25]. This synergy endows CNFs with considerable strength and high-order radial deformation modes[4,26]. However, due to random and unconstrained nucleation, the spatial distribution of nanocrystals is challenging to regulate, often resulting in grain aggregation and interleaving[4,6,24,25]. This often-overlooked phenomenon could be the key factor limiting DP CNFs from attaining higher strengths and even RT plasticity[27,28]. Under high load, intercrystalline stress concentrations within nanocrystal clusters would initiate cracks that propagate rapidly, leading to fracture before plastic yielding[22,23]. Furthermore, the lethal impact of cross-scale defects caused by conventional fabrication methods on the comprehensive mechanical performance of CNFs is also underestimated[29]. Here, we report a nucleation regulation strategy for crystalline/amorphous DP CNFs to achieve high strength,

superior flexibility, and RT plasticity synchronously. The resulting unique DP structure, possessing reduced nanocrystal aggregation, increased internal interfaces, and the elimination of fiber defects, is realized through the interface-induced nucleation together with a newly designed template-free electrospinning method. TiO_2, a widely used ceramic known for its excellent physicochemical properties, but brittle and weak nature, serves as the proof-of-concept model in this study. Structural characterizations and single-nanofiber mechanical tests highlight that these structural optimizations effectively mitigate localized stress concentrations across scales, fully activating the synergistic advantages and multiple deformation mechanisms of DP configurations, thereby improving the comprehensive mechanical properties of CNFs.

Results
Conceptual design
The amorphous/crystalline DP structure provides an optimal platform for simultaneously enhancing the mechanical properties of CNFs. Herein, we devised reconfiguration and optimization schemes of DP CNFs for stress analysis and evaluation (Fig. 1a). The construction of Model-1 is based on DP CNFs obtained by the typical electrospinning process, characterized by fiber defects resulted from the thermal decomposition of organic templates during fabrication. Model-2 improves upon Model-1 by eliminating fiber defects, but significant localized aggregation persists due to the random and unconstrained growth of nanograins. Model-3, in contrast, not only eradicates multiscale defects but also prevents nanograin aggregation. In engineering applications, tensile strength (σ), axial strain (ε), and flexibility are key mechanical attributes of single CNFs. The σ and ε of CNFs are directly related to the deformation mechanisms under tensile load (Fig. 1b). Regarding bending deformations, these can be understood as a coupling of compressive (inner side) and tensile (outer side) behaviors along the fiber axis at the microscale[7,30]. Due to the intrinsic nature of ceramics, where compressive endurance generally exceeds tensile endurance, the flexibility of CNFs is thus dominated by their localized tensile behavior.

Owing to the high aspect ratio (>1000), CNFs exhibit an uneven distribution of tensile σ along the axial direction, which conforms to the Weibull model. According to the Weakest Link theory[31,32], the mechanical properties of CNFs depend on their most fragile sections. For Model-1, structural defects such as pores, cracks, and voids are the limiting factors for mechanical performance. These defects are highly prone to stress concentration under tensile load, leading to catastrophic fractures that largely negate the advantages of the DP structure. Consequently, eliminating structural defects in Model-2 is expected to effectively improve mechanical properties, provided that the limitations of current fabrication methods are addressed. However, upon reaching certain thresholds of σ or ε, the fragile grain boundaries between aggregated nanograins may undergo stress concentration and crack initiation, hindering further mechanical optimizations. Similarly, nanocrystal clusters located on the surface of CNFs will also weaken the flexibility of Model-2. In contrast, Model-3 possesses no detrimental nanocrystal aggregation and increased internal interfaces. This optimized spatial distribution allows Model-3 to fully leverage the synergistic advantages of the DP structure, achieving superior σ and flexibility.

Regarding deformability, we constructed molecular dynamics (MD) models and performed tensile simulations. We utilized LAMMPS and the Matsui-Akaogi force field to successfully construct various TiO_2 models, including amorphous and DP structures (Fig. 1c, d). The Matsui-Akaogi force field has been validated as one of the most appropriate for describing TiO_2[33–35]. In the radial distribution function (RDF) of DP TiO_2, peaks located at ~1.99 Å in the Ti−O curve, and at ~3.15 Å and ~3.89 Å in the Ti−Ti curve, highlight its hypocrystalline features (Fig. 1e). For different DP configurations, Model-2 represents
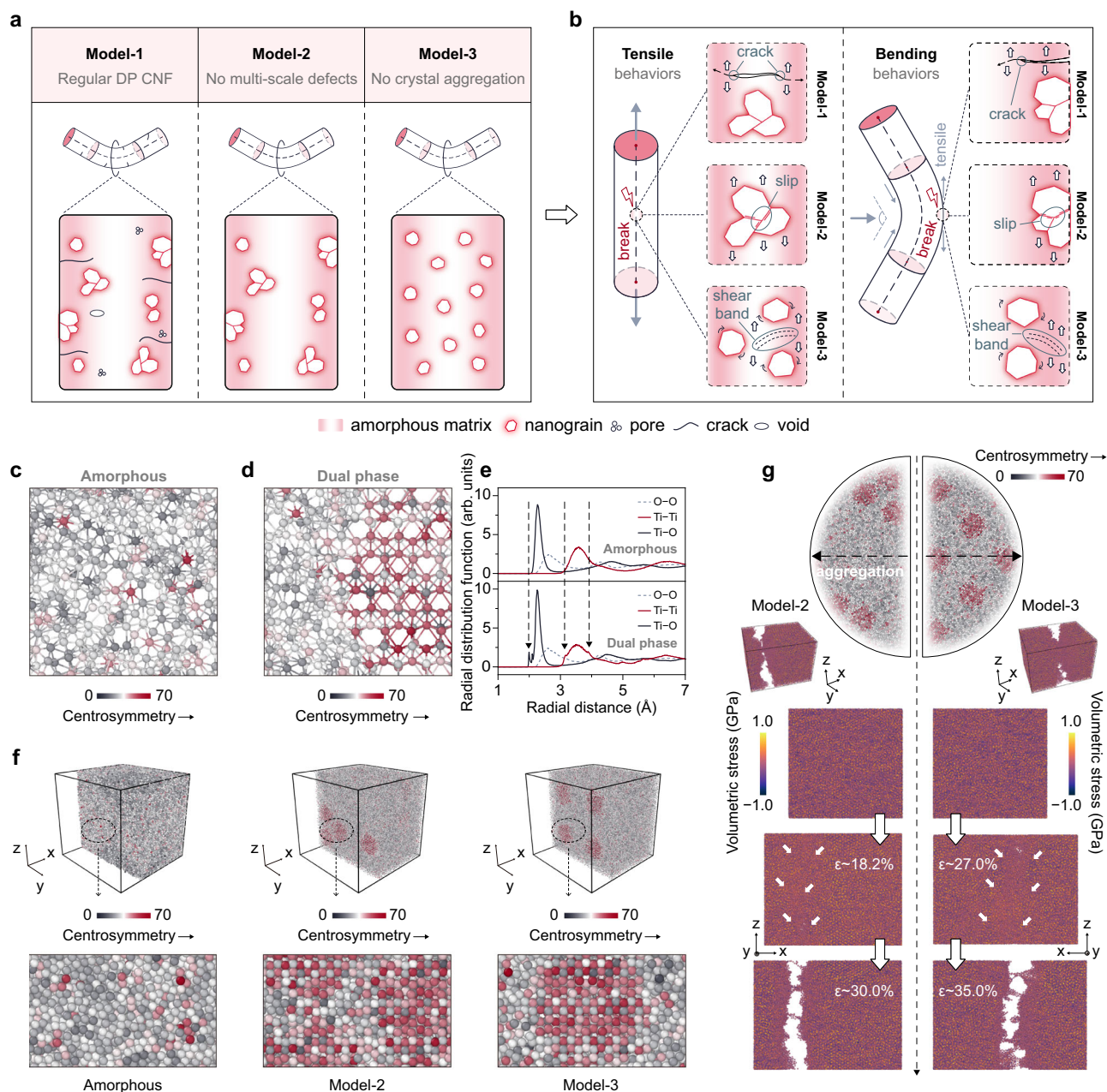
Fig. 1 | Conceptual design of dual-phase (DP) ceramic nanofiber (CNF). a Three distinct models of DP CNFs and their differences. Model-1 represents DP CNFs fabricated by conventional methods, characterized by structural defects and uncontrolled crystal distribution. Model-2 eliminates multiscale structural defects, while Model-3 not only removes these defects but also prevents crystal aggregation. **b** Stress analysis and fracture mechanisms of DP CNFs under tensile and bending loads. During tensile deformation, Model-1 fractures would originate from structural defects, while Model-2 fails as a result of slip at the inner interfaces within nanocrystal clusters. In contrast, Model-3 overcomes these limitations and

undergoes deformation until shear bands develop in the amorphous region, leading to fracture. During bending deformation, the fracture mechanism is dominated by localized tensile behavior on the outer side. **c**–**d** Molecular dynamics (MD) models for amorphous TiO_2 and DP TiO_2 with the color scale bar indicating the centrosymmetry parameter for each atom in the system. **e** Radial distribution functions for Ti–O, Ti–Ti, and O–O bonding in amorphous and DP TiO_2 models, respectively. **f** Construction of MD models for the amorphous structure, Model-2, and Model-3. **g** Snapshots at different strains (ε) during tensile simulations of Model-2 and Model-3, with the color scale bar representing the volumetric stress.

nanocrystal aggregation, whereas Model-3 features uniformly distributed nanograins. Tensile simulations were then performed on Model-2 and Model-3 to investigate differences in their mechanical behaviors (Fig. 1f, g)[6,27,36,37]. We observed that the fracture location in Model-2 corresponds to areas of nanograin aggregation (Supplementary Fig. 1), supporting the hypothesis that fracture initiates at the grain boundaries within nanocrystal clusters. In contrast, the fracture in Model-3 occurs in amorphous regions, which is typically associated with localized stress concentrations by shear bands, indicating that the

structural optimizations in Model-3 alter its fracture mechanism (Supplementary Fig. 2)[26,38–40]. Firstly, the risk of crack initiation due to tearing between nanograins is significantly reduced in Model-3[7,12]. Secondly, the spatial independence of nanograins may allow them to absorb energy through slip and rotation behaviors[26]. Moreover, the amorphous matrix gains better structural continuity and would act as a soft boundary to transfer and dissipate stress[4,27]. These multiple deformation mechanisms benefit to delay the onset of fracture in CNFs until plastic deformation occurs.

CNF synthesis

To precisely achieve the respective structures of Model-1, Model-2, and Model-3, we designed distinct synthesis approaches. Model-1 can be readily produced using conventional fabrication processes. However, fabricating Model-2 presents challenges, as CNF formation heavily relies on polymer templates to assist electrospinning, whose decomposition during sintering inevitably introduces multi-scale defects into CNFs[29,41]. To address this issue, we developed an approach to synthesize spinnable linear particle sols based on a ligand-exchange molecular design, allowing template-free electrospinning to eliminate subsequent fiber defects. On this basis, we combined template-free electrospinning with an interface-induced nucleation strategy to realize Model-3, by modulating the form and spatial distribution of nanograins.

Specifically, we engineered a ligand-exchange route based on coordinated modification to tailor the electronic structures and steric hindrances of Ti alkoxides, thus controlling their activity and polymerization to synthesize spinnable linear particle sol (LP-sol) (Fig. 2a). Metal alkoxides, as reactive monomers, owing to their polyfunctionality and expandable orbitals of central ions, tend to polymerize rapidly and branch extensively, forming an irreversible 3D network (Supplementary Fig. 3)[42–44]. The resultant spherical particle sol (SP-sol) possesses no spinnability, as observed in the conventional synthesis route. Hence, to curb the branching tendency and high reactivity of Ti alkoxides (such as titanium butoxide), we introduced multidentate ligands such as HOAc to modify the monomer structure (Supplementary Fig. 4)[44–46]. By adjusting the molar ratio (r_m) of ligand to monomer, we effectively manipulated their coordinated structures (Supplementary Fig. 5), which involves three different coordination protocols (Fig. 2b)[47,48]. However, excessive modification can terminate the hydrolysis-condensation reactions of the monomers. To strike a balance, we conducted the spinnability assessments (Supplementary Fig. 6) to identify the optimal r_m range (1.0-2.0). Based on this, combined with a well-designed process, the polycondensation of monomers proceeds in an approximately linear mode, as confirmed by tracking sol rheology during the reaction. We measured the apparent viscosity (η) as a function of relative time (t/t_g, t is the reaction time and t_g is the time for gel formation), where the relationship between $\ln(\eta)$ and $\ln[(t/t_g)/(1 - t/t_g)]$ clearly divides the LP-sol synthesis process into two distinct stages (Supplementary Fig. 7). After reducing pressure, the fitted curve conforms to a linear relationship with a high slope, implying rapid and chain-like condensation of the modified monomers[49,50]. For deeper insights, we extracted the reduced viscosity (η_{sp}/C) as a function of concentration (C) during LP-sol polycondensation (Fig. 2c), which follows the Huggins equation:

$$\eta_{sp}/C = [\eta] + k[\eta]^2 C \qquad (1)$$

where k is a proportionality constant and $[\eta]$ is the intrinsic viscosity[51]. The monotonic increase in slopes underscores the linear growth of particles in LP-sol[52]. As a contrast, the C-independent η_{sp}/C in SP-sol reflects the spherical shape of its particles, as described by the following formula:

$$\eta_{sp}/C = 0.025/\rho \qquad (2)$$

where ρ is the particle density[53]. Notably, LP-sol exhibits optimal spinnability and shear thinning at $t/t_g = 0.8$, whereas the non-spinnable SP-sol consistently behaves as a Newtonian fluid (Fig. 2d). These findings highlight that the spinnability of LP-sol originates from the linear polycondensation of modified monomers and their resulting rheological properties. In brief, Model-2 was synthesized from LP-sol ($t/t_g = 0.8$), while Model-1 was fabricated by combining SP-sol with a polymer template.

Despite this, the template-free electrospinning strategy is insufficient for realizing Model-3, as it fails to regulate crystal nucleation and growth. Inspired by recent in-situ observations of crystallization, we combined SP-sol with LP-sol in electrospinning, thereby embedding nanoclusters within the precursor fibers (Fig. 2e)[54–56]. This pre-configuration offers an intriguing binary amorphous structure: a matrix composed of loosely stacked Ti−O chains, and dense nanoclusters formed by a cross-linked Ti−O network. In the electrostatic field, double-layer repulsion and charged jet whipping could facilitate the dispersed migration of nanoclusters[15]. In the thermal field, the binary amorphous interfaces within the precursor would induce the nucleation and growth of nanograins. Admittedly, incorporating SP-sol into LP-sol will negatively affect the sol spinnability and the morphology of precursor fibers (Supplementary Table 1). To address this, we optimized the binary sol composition to 5 wt% SP-sol and 95 wt% LP-sol which demonstrates superior entanglement-relaxation behavior, precursor morphology, and abundant nanoclusters (Supplementary Fig. 8)[57]. Besides, we compared the key rheological properties of SP-sol, LP-sol, and the binary sol, including non-Newtonian index (n), yield stress (τ), and $[\eta]$, based on the Power-law model, Huggins equation, and Casson plots, respectively. The structural and rheological properties of the binary sol ($n \sim 0.87$, $\tau \sim 13.7$ mPa, $[\eta] \sim 0.23$ dL g^{-1}) are almost completely inherited from LP-sol. Similarly, in terms of storage modulus (G') and loss modulus (G''), the viscoelastic properties of the binary sol are akin to LP-sol rather than SP-sol (Supplementary Fig. 9). We then investigated the effect of implanted nanoclusters on the crystallization of DP CNFs. By analyzing gradient non-isothermal differential scanning calorimetry (DSC) curves (Supplementary Fig. 10), we calculated the activation energy (ΔG_a) for the amorphous-to-anatase transition based on the modified Avrami equation:

$$\ln\left(T_p^2/h\right) = \Delta G_a/\left(RT_p\right) + \ln(\Delta G_a/R) - \ln\upsilon \qquad (3)$$

where R is the gas constant, T_p is the peak temperature, h is the heating rate, and υ is the frequency factor[58]. Apparently, the internal interfaces formed between the implanted nanoclusters and the matrix facilitate crystallization (Fig. 2f), as evidenced by a -69.58 kJ mol^{-1} reduction in ΔG_a (Fig. 2g). It can be inferred that the embedded nanoclusters promote skipping early phase-separation and fusion stages (Supplementary Fig. 11), inducing nucleation at the internal interfaces (Fig. 2h), which is important to avoid the gathered growth of nanocrystals[54,55,59,60]. X-ray diffraction (XRD) patterns display the phase structure evolution of the binary pre-configuration (Fig. 2i) compared to its counterparts without embedded nanoclusters (Supplementary Fig. 12). Eventually, Model-3 was synthesized by combining SP-sol and LP-sol.

Structural analysis

Through a series of structural characterizations and comparisons, we confirmed the successful construction of DP structures corresponding to Model-1, Model-2, and Model-3 (Fig. 3a). Morphological observations reveal a rough surface and a loosened interior in Model-1, in stark contrast to the dense structures of Model-2 and Model-3 (Fig. 3b and Supplementary Fig. 13). Porosity analysis using the Brunauer-Emmett-Teller (BET) theory shows that Model-2 and Model-3 display type II adsorption-desorption isotherms, indicating the non-porous nature (Fig. 3c)[61]. Conversely, a type IV isotherm with hysteresis loop and capillary condensation is found in Model-1, along with a higher BET surface area ~42.62 m^2 g^{-1} (Supplementary Fig. 14). The specific surface area calculated from BET theory is based on the multilayer gas adsorption model. For verification, Langmuir theory, which assumes monolayer gas adsorption[62,63], was also applied. The Langmuir surface area results show the same trend, with Model-1 exhibiting a notably larger surface area than Model-2 and Model-3, consistent with the BET findings. Compared to the non-porous structures of Model-2 and Model-3, the mesopores and micropores in Model-1 would serve as the
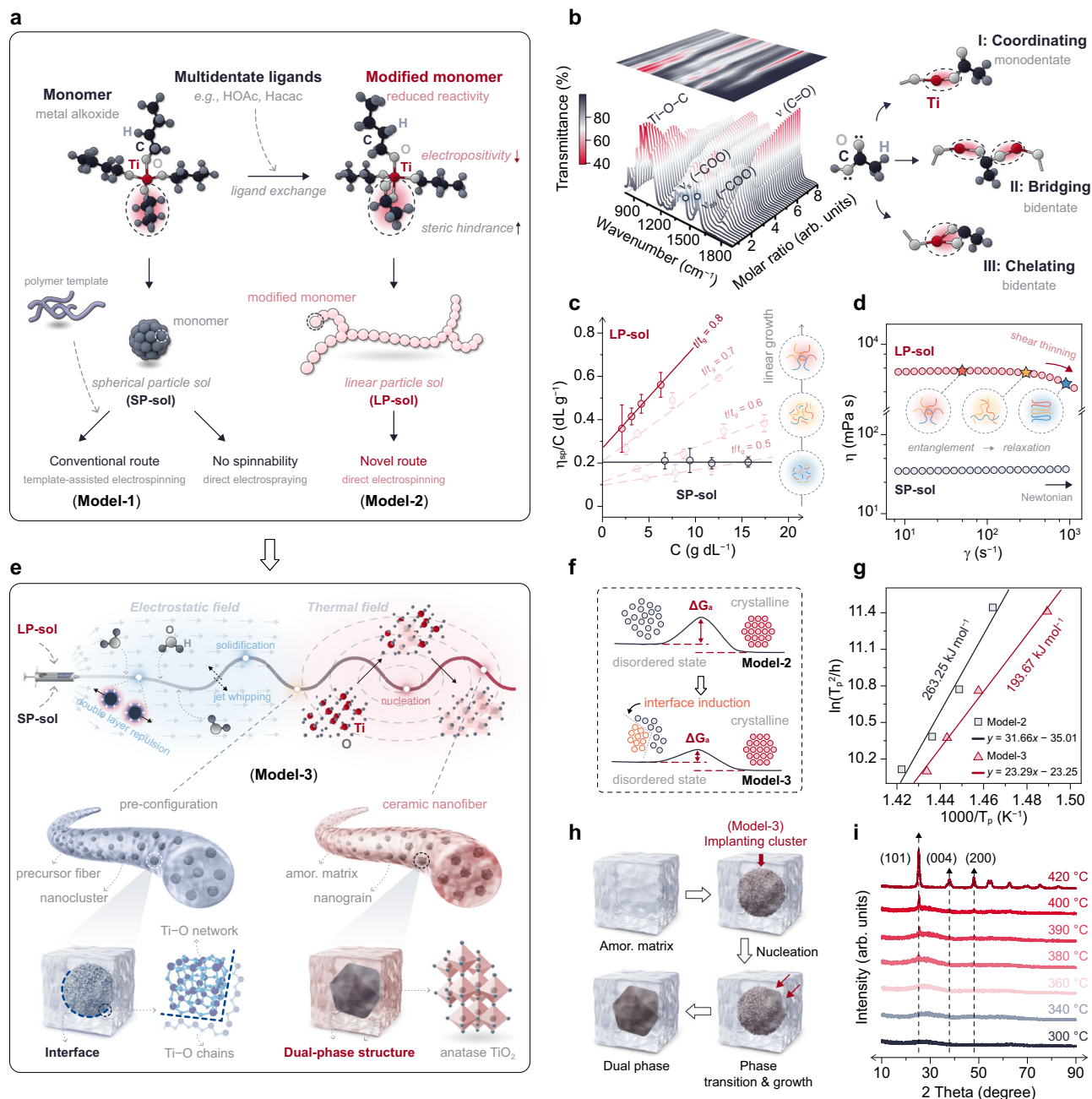
Fig. 2 | Synthesis process. a Schematic diagram illustrating the synthesis of spherical particle sol (SP-sol) and linear particle sol (LP-sol). **b** Molecular structures of modified monomers with different molecular ratio (r_m), analyzed by Fourier-transform infrared spectroscopy. Coordination protocols include: I. monodentate coordination, II. bidentate bridging, and III. bidentate chelating. **c** Relationship between reduced viscosity (η_{sp}/C) and concentration (C) for SP-sol, and LP-sol ($r_m = 1.5$) obtained at different relative times (t/t_g). Each data point represents the average of five samples, with error bars indicating the standard deviation. The fitting lines for LP-sol have coefficient of determination (R^2) values of 0.999 ($t/t_g = 0.5$), 0.978 ($t/t_g = 0.6$), 0.981 ($t/t_g = 0.7$), and 0.992 ($t/t_g = 0.8$). The fitting line for SP-sol has an R^2 value of 0. **d** Plots of apparent viscosity (η) versus shear rate (γ)

for SP-sol and LP-sol ($t/t_g = 0.8$). Inset: entanglement-relaxation behavior of linear particles. **e** Schematic illustrating the interface-induced nucleation and synthesis of Model-3. **f** Reduction in activation energy (ΔG_a) due to the binary phase interface of the pre-configuration. **g** Avrami plots (T_p and h represent the peak temperature and the heating rate, respectively) derived from gradient non-isothermal differential scanning calorimetry, used to calculate the ΔG_a for the amorphous-to-crystalline transition before and after nanoclusters implantation in the precursor. The R^2 values of the fitting lines are 0.968 (Model-2) and 0.993 (Model-3), respectively. **h** Implanted nanoclusters promote nucleation localized at the binary interfaces. **i** X-ray diffraction patterns showing the phase structure evolution of the binary pre-configuration for Model-3.

weakest link (Fig. 3d), rendering it more prone to fracture under load. These porosities predominantly form during the sintering stage of the CNFs, driven by the evolution of constituents and structural defects. Thus, we further examined the sintering process through thermo-analytical methods. Thermogravimetric analysis (TGA) and derivative curves disclose complex weight-loss behaviors in Model-1, including solvent volatilization, thermal condensation, polymer decomposition,

and nucleation-crystallization stages (Supplementary Fig. 15)[7]. Between 438.84 °C and 509.11 °C, a rising-plunging trend is observed in the TG curve of Model-1, which could be attributed to the oxidation of residual carbon and subsequent gas release. As the gases diffuse and escape, they would leave behind pathways to behave as structural defects. Furthermore, Model-1 exhibits weight loss termination at ~538.44 °C, markedly later than Model-2 (~344.15 °C) and Model-3
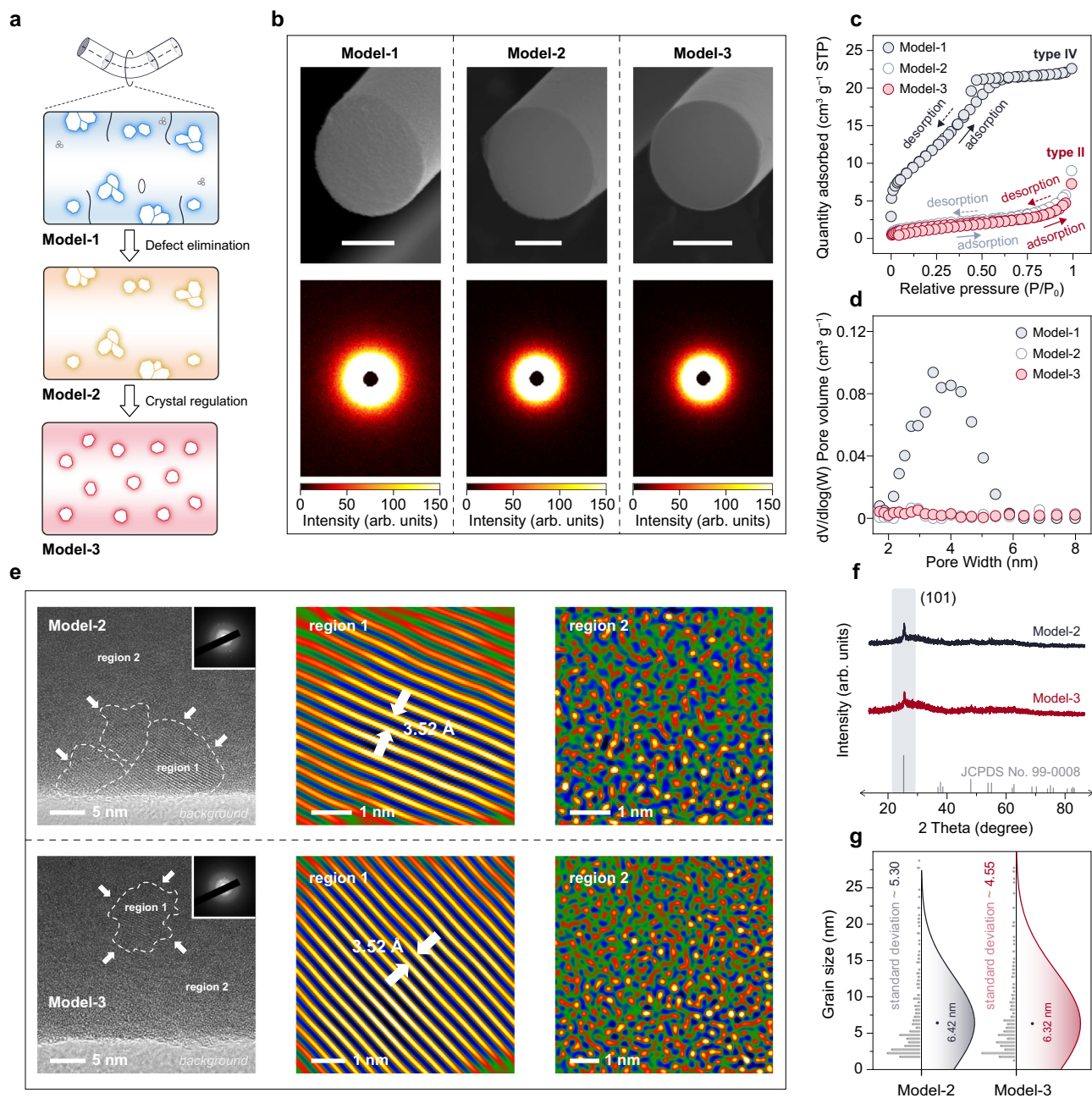
Fig. 3 | Structural comparison. a Schematic illustration highlighting the differences among Model-1, Model-2, and Model-3. Here, Model-2 was obtained by eliminating the multiscale defects of Model-1 via the template-free method. Model-3 was then achieved by preventing the nanocrystal aggregation through the nucleation-regulation strategy. **b** Field emission scanning electron microscopy images showing cross-sectional morphologies (scale bar = 200 nm) of Model-1, Model-2, and Model-3 (top). Small-angle X-ray scattering patterns of Model-1, Model-2, and Model-3 (bottom). **c** N₂ adsorption-desorption isotherms. **d** Pore size distribution curves. **e** High-resolution transmission electron microscopy observations (inset: selected area electron diffraction patterns) of Model-2 and Model-3, and the fast-Fourier-transform images of amorphous and crystalline regions, respectively. **f** X-ray diffraction patterns of Model-2 and Model-3, all showing the sharp peak at ~25.5°, corresponding to the (101) plane of anatase. **g** Size distributions of nanograins in Model-2 and Model-3, based on statistical analysis, exhibiting similar average sizes but differing levels of uniformity.

(-339.35 °C). These discrepancies point to the overlapping temperature regions for polymer decomposition and DP structure incubation in Model-1. Further insights from small-angle X-ray scattering (SAXS) corroborate these findings, with the highest scattering intensity exhibited in Model-1 (Supplementary Fig. 16). As shown in Fig. 3b, the SAXS 2D pattern of Model-1 demonstrates extra scatterers, potentially attributed to the internal pores[29]. Hence, the template-free electrospinning method is effective for decoupling DP structure incubation from the removal of organic components, which is vital for eliminating fiber defects.

On the other hand, we delved into the effects of implanted nanoclusters on the eventual crystal structure of the CNFs. Although both Model-2 and Model-3 display the crystalline/amorphous DP structure, their spatial arrangements of nanograins and amorphous matrices differ significantly. Model-2 predominantly exhibits surface-focused crystallization and aggregated nanograins, whereas these phenomena are rarely detected in Model-3 (Fig. 3e). The nanocrystal clusters in Model-2 contain numerous fragile inner grain boundaries, which are prone to sliding and tearing under loads. In contrast, the modulated nanograins in Model-3 show optimized spatial

independence, which not only facilitates the full exploitation of the synergistic advantages of the DP structure but also encourages multiple deformation mechanisms. The composition and phase constitution of Model-2 and Model-3 are identical, as evidenced by nanocrystals exposing the (101) plane, surrounded by a disordered atomic arrangement. Their electron diffraction patterns both exhibit coupling of amorphous halos and crystalline spots, consistent with the hypocrystalline features identified in their XRD patterns (Fig. 3f and Supplementary Fig. 17). Thus, the distinctions between the synthesized DP CNFs primarily lie in the form and spatial distribution of nanocrystals, aligning with the theoretical models. Due to thermal gradients along the radial direction of the precursor fiber, the nucleation of the disordered matrix is spatially uneven, which is then altered by the construction of binary interfaces. Typically, nanograin formation would undergo stages of phase separation, fusion, nucleation, and growth, as mentioned in Supplementary Fig. 11, then readily developing into nanocrystal clusters. However, the binary interfaces in the Model-3 precursor may encourage skipping the early phase-separation and fusion stages, inducing nucleation at the binary interface with a reduced ΔG_a as mentioned in Fig. 2g, thus dominating the growth and spatial distribution of nanocrystals[54,55,59,60]. Such interface-induced nucleation effect also optimizes the size distribution of nanograins (Fig. 3g), as the uniformity of Model-3 (standard deviation ~ 4.55) outperforms that of Model-2 (standard deviation ~ 5.30). This optimized DP configuration increases internal interfaces, endowing the amorphous matrix better structural continuity and reducing the risk of crack initiation caused by intercrystalline stress concentration. These structural analyses underscore the successful experimental synthesis of Model-1, Model-2, and Model-3.

Single-nanofiber mechanics

Focusing on the initial goal of synchronously enhancing the comprehensive mechanical attributes of CNFs, we conducted a series of in-situ mechanical tests to evaluate the performances of Model-1, Model-2, and Model-3. Given the difficulty of manipulating a single CNF, tensile tests were performed using a specialized push-to-pull (PTP) device (Fig. 4a), which converted the indentation load into uniaxial stress along the fiber axis[26,29,41]. By employing focused ion beam (FIB) techniques, individual CNFs were precisely cut and fixed within the specimen area (tensile gap ~ 2.5 μm). The force-displacement relation and corresponding real-time movies were dynamically recorded (Supplementary Movies 1-3), and stress-strain curves were extracted (Fig. 4b), exhibiting an increase until yielding or fracture occurred (Fig. 4c). For Model-1, the ultimate σ (σ_u) is ~0.16 GPa, and the total ε (ε_{sum}) reaches ~2.61%. These unsatisfactory performances are unsurprising, since the fiber defects and the intrinsic TiO_2 brittleness counterbalance the benefits of DP structure. On the other hand, much superior mechanical properties are observed in Model-2 (σ_u ~ 0.82 GPa, ε_{sum} ~ 7.43%) and Model-3 (σ_u ~ 1.06 GPa, ε_{sum} ~ 8.44%), among which the latter is notable for exceeding the highest values reported so far in TiO_2 nanofiber (σ_u ~ 0.80 GPa, ε_{sum} ~ 5.00%)[9]. Thus, the elimination of multi-scale defects significantly improves the mechanics of crystalline/amorphous DP CNFs, underscoring the severe underestimation of the lethal impact of conventional CNF fabrication methods.

In addition to σ_u and ε_{sum}, distinct deformation modes are displayed in Model-1, Model-2, and Model-3 under external loads. Conventional ceramics lack plastic deformation upon tensile loading at room temperature, as shown in the stress-strain curve of Model-1, with ~2.61% of elastic ε (ε_e) and ~0% of plastic ε (ε_p). Surprisingly, we observed extraordinary plastic behaviors in Model-3 (ε_e ~ 5.34% and ε_p ~ 3.10%). Owing to the accumulation of recoverable interatomic bonding elongation, Model-3 initially reaches its elastic ε limit. After the ε threshold (~5.34%), yielding and strain hardening occur. Notably, the fracture σ (σ_f) of Model-3 is ~1.04 GPa, lower than its σ_u, indicating a

stage of non-uniform plastic deformation, and implying a potential multiple deformation mechanism, which distinguishes it from Model-2 ($\sigma_u = \sigma_f$). Such a finding is particularly noteworthy because the ductility-related behaviors observed in Model-3 are a typical characteristic of metals, yet are rarely associated with ceramics[22]. Besides the remarkable plastic deformation, the elimination of defects and modulation of internal interfaces dramatically enhances the toughness of Model-3 (~58.45 MJ m^{-3}), which is ~32.11 times and ~1.79 times greater than that of Model-1 and Model-2, respectively (Supplementary Fig. 18). Additionally, the dense nature and optimized DP configuration render a higher Young's modulus in Model-3 (~20.66 GPa), surpassing that of Model-1 and Model-2 as well (Supplementary Fig. 19).

We further assessed the flexibility of single CNFs by determining the radius of curvature (R_c) at their critical bending limits (Supplementary Movies 4–6). Specifically, one end of each CNF was fixed to a substrate and the other was attached to a movable probe, which bent the fiber until fracture to calculate R_c (Fig. 4d and Supplementary Fig. 20). It shows the R_c for Model-1 and Model-2 are ~7.65 μm and ~2.37 μm, respectively, much higher than that of Model-3 ($R_c < 0.47$ μm) (Fig. 4e). A lower R_c indicates greater flexibility due to a higher rotation rate of the tangent direction relative to the arc[64]. In particular, comparing Model-2 and Model-3 reveals the importance of nanograins distribution in CNF flexibility, as the grain aggregation around the fiber surface would serve as the stress concentration zone and weaken the bending limits. These in-situ mechanical tests confirm the comprehensive mechanical optimization in Model-3, including enhanced σ_u, ε_p and R_c, primarily due to the elimination of multi-scale defects and the modulation of the DP structure. Also, these mechanical characteristics were further validated through additional in-situ tests (Supplementary Fig. 21 and Fig. 22).

Building on the mechanical tests, structural characterizations, and theoretical simulations, we discussed the origin of the exceptional comprehensive mechanical performance of Model-3. Due to the elimination of multi-scale defects and the regulation of internal interfaces, the synergistic advantages of the DP structure are fully exploited, as demonstrated by the stress analysis showing a stable configuration (Fig. 4f)[6,24,26]. Moreover, unlike Model-2, which has many fragile inner grain boundaries within its nanograin clusters (Fig. 4g), Model-3 reduces the risk of boundary tearing and crack propagation, achieving further enhancements in σ, ε_p, and R_c (Fig. 4h). Upon reaching the tensile threshold, Model-3 may proceed to multiple deformation mechanisms. The spatial independence of nanograins could allow absorbing energy through slip/rotation behaviors, involving bond-switching events at the phase interfaces[3,65,66]. The XPS O 1s spectra reveal the presence of oxygen vacancies in Model-3, implying a number of dangling bonds within the structure (Fig. 4i and Supplementary Fig. 23)[67]. It is reported that the bond-switching events can be initiated by these vacancy defects and dangling bonds, which are beneficial in improving the deformation potential of oxide ceramics[68,69]. On the other hand, the enhanced structural continuity of the disordered matrix, combined with the stabilizing effect of the nanocrystals, allows for improved stress transfer and dissipation, likely delaying the onset of shear band formation. These multiple deformation modes encourage the plasticity before the CNFs fracture. Eventually, as mentioned in Fig. 1g, Model-3 may fracture due to localized stress concentration within shear bands in the amorphous regions, rather than initiating in the nanocrystal domains[26,38–40]. Altogether, Model-3 integrates high strength, RT plasticity, and superior flexibility, breaking through the intrinsic contradiction between different mechanical properties. This comprehensive optimization of key mechanical attributes enables CNFs to effectively absorb energy and transfer loads, thus facilitating their aggregate materials (Fig. 4j) to demonstrate remarkable macroscopic performance by avoiding stress concentration and maintaining structural stability (Fig. 4k–n).
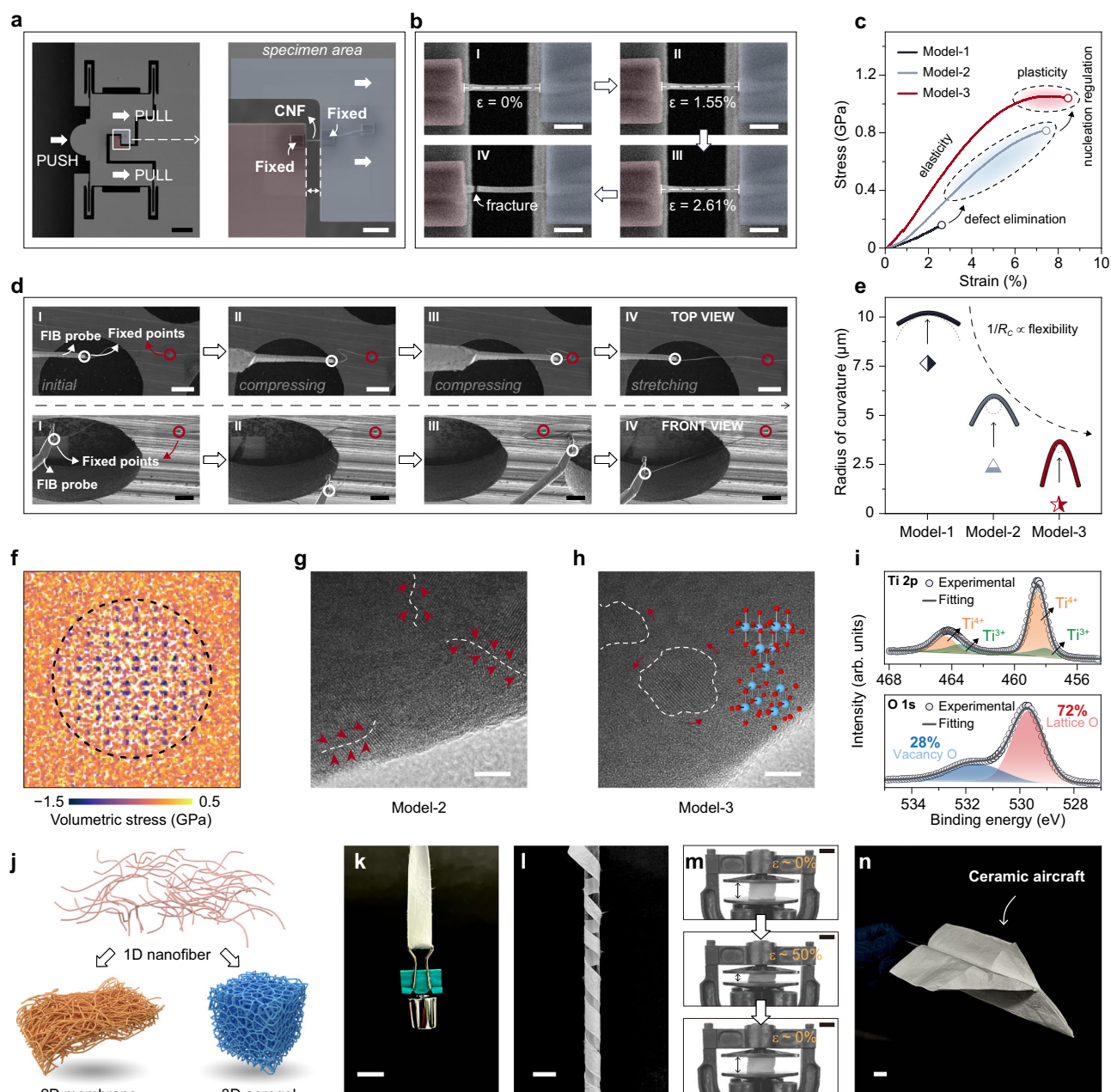
Fig. 4 | Mechanical tests. a Details of the in-situ tensile test, including the architecture of the PTP devices (left, scale bar = 50 µm) and a high-magnification view of the specimen area (right, scale bar = 5 µm). **b** Snapshots from real-time movies capturing the entire tensile process (Model-1, scale bar = 1 µm). **c** Extracted stress-strain curves for Model-1, Model-2, and Model-3. **d** Details of the in-situ bending test, showing top view (top) and front view (bottom) during manipulation, where one end of the ceramic nanofiber (CNF) was fixed to a substrate and the other to a movable probe, then bent to determine the lowest radius of curvature (Model-3, scale bar = 10 µm). **e** Extracted radius of curvature (R_c) for Model-1, Model-2, and Model-3. Inset: schematic diagram of a single CNF showing different rotation rates of the tangent direction relative to the arc. **f** Stress field distribution in the nanocrystal region and its surrounding of the dual-phase structure (Model-3). The color scale represents the volumetric stress of each atom in the simulated system. **g**–**h** High-resolution transmission electron microscopy observations of Model-2 and Model-3 (scale bar = 10 nm). Inset: nanocrystals in the anatase form, with blue spheres representing Ti atoms and red spheres representing O atoms. **i** X-ray photoelectron spectroscopy analysis of the O 1s and Ti 2p spectra of Model-3. **j** Strategic assembly of Model-3 into two-dimensional (2D) membranes and three-dimensional (3D) aerogels, demonstrating macroscopic properties (scale bar = 1 cm): **k** high strength, **l** flexibility, and **m** compressibility. **n** Integration of high strength, superior flexibility and plasticity in CNFs enables the membrane to be folded into the shape of an aircraft (scale bar = 1 cm).

Discussion

For applications with extreme mechanical environments, ceramic components are required to exhibit high strength, flexibility, and even plastic deformation. We have proved that the template-free synthesis method, combined with an interface-induced nucleation strategy, offers a promising solution to meet these demands. From a macroscopic perspective, we investigated how the mechanical integrations of single CNFs, including tensile strength, axial strain limit, and flexibility, affect the performances of the aggregates derived from them. For instance, the strategic assembly of CNFs into 3D aerogels revealed that those composed of synthesized Model-3 exhibit superior elasticity and structural stability compared to those of Model-1 and Model-2 (Supplementary Fig. 24). Notably, single-fiber defects are also fatal to the macroscopic mechanics, as

evidenced by the collapse of the aerogel with Model-1 as the structural unit after only compressive $\varepsilon \sim 20\%$, compared to the $\varepsilon \sim 80\%$ that Model-3 can robustly withstand. Observations of the macroscopic behavior of aggregates underscore the importance of improving the comprehensive mechanics of single CNFs, since which collectively determine their ability to absorb energy and transfer loads as structural units. In the future, further efforts toward optimizing the mechanical properties of single CNFs are anticipated. One potential avenue is utilizing Model-3 as a platform to systematically modulate the size and quantity of nanograins (Supplementary Fig. 25), thereby gaining insights into how the volume fraction of the nanocrystal domain affects the evolution of the DP structure under loading. Accelerating this process could benefit from the incorporation of effective medium theories[70]. With appropriate modifications, these classical theories are expected to simplify structure-mechanics relationships and offer predictive and guiding information. Another promising direction lies in the patterned design or orderly arrangement of nanocrystal regions within amorphous matrices. A more ordered and uniform distribution is predicted to suppress shear-band activation, and meanwhile constrain the migration and bypassing of disordered atomic clusters, thereby further promoting the mechanical strength and strain limits[27].

In summary, we have demonstrated the extraordinary integration of high strength, superior flexibility, and RT plasticity in single CNFs. This achievement originates from the optimized crystalline/amorphous DP structure, characterized by reduced nanograin aggregation, increased internal interfaces, and the elimination of fiber defects. These structural reconfigurations effectively mitigate multi-scale stress concentrations in single CNFs, fully activating the synergistic advantages and multiple deformation mechanisms of the DP structure. Such a remarkable integration of mechanical attributes is unprecedented in conventional ceramic materials, and opens up opportunities for CNFs in various extreme scenarios, including mechanical shocks, high-frequency vibrations, and repeated twisting. Furthermore, this comprehensive and "no-weak-links" mode to mechanical enhancement may also serve as a guide for the widespread industrialization of CNFs in the future.

Methods

Synthesis of sols

The preparation of SP-sol involved the following steps. Initially, ethanol (EtOH), deionized water (H_2O), acetic acid (HOAc), and hydrochloric acid (HCl) were mixed adequately in a r_m of 10:4:0.5:0.5. This mixture was stirred continuously at room temperature with a stirring rate of 200 rad min^{-1} to obtain solution (I). Subsequently, titanium butoxide (TBT), in a molar quantity equal to one-quarter of the total H_2O in the reaction system, was carefully and slowly added to the solution (I). Finally, the mixture was stirred continuously for 2 h at room temperature to yield SP-sol. Regarding the LP-sol synthesis, HOAc and TBT were mixed in an example of $r_m = 1.5$:1, and the mixture was diluted with an equal volume of butanol (BuOH), forming solution (II). These were then stirred at room temperature with a stirring rate of 200 rad min^{-1} for 8 h. It was crucial to strictly avoid any H_2O contamination throughout the reaction. Further, a mixture of H_2O and 10 times its volume of BuOH was vigorously shaken to form solution (III), with a r_m of TBT to H_2O of 1:1. Afterwards, solution (III) was carefully added dropwise to solution (II), and the mixture was stirred continuously at 60 °C with a stirring rate of 200 rad min^{-1} for 2 h. The reaction mixture was subsequently heated to 80 °C and concentrated under reduced pressure (vacuum of −0.1 MPa), while stirring at 200 rad min^{-1} until a spinnable LP-sol was obtained. Ultimately, the binary sol was engineered by mixing SP-sol and LP-sol at a specific mass ratio. For instance, SP-sol and LP-sol were thoroughly mixed at a mass ratio of 1:19, and the mixture was continuously stirred at room temperature with a stirring rate of 200 rad min^{-1} for over 1 h to achieve binary sol (5 wt% SP-sol).

Fabrication of CNFs

Model-1 synthesis required polyvinylpyrrolidone (PVP, molecular weight = 1,300,000) as a polymer template to assist with electrospinning. PVP (3.2 wt% of sol solution) was added to the vigorously stirring SP-sol (200 rad min^{-1}) until fully homogenized, then allowed to rest for 1 h before use. Electrospinning was performed under controlled conditions (25 ± 2 °C and 40 ± 2% RH) employing an electrostatic voltage of 15-30 kV and maintaining a distance of 15 cm between the needle tip and the collector. The spinning solution was fed at a rate of 0.5-3.0 mL h^{-1} to form precursor fibers. These fibers were then sintered at 380-420 °C for 1 h with a heating rate of 2 °C min^{-1} to obtain Model-1. The preparation of Model-2 ($t/t_g = 0.8$) and Model-3 involved no polymer templates. Their electrospinning parameters could refer to those used for Model-1. Finally, their corresponding precursor fibers were sintered at 380-420 °C (2 °C min^{-1}) to obtain Model-2 and Model-3, respectively.

Characterizations

The rheological properties of the samples were characterized using a Thermo Scientific HAAKE Viscotester iQ Air Rheometer. FT-IR spectra were obtained using a Nicolet 6700 spectrometer from Thermo Fisher Scientific to identify functional groups and chemical bonding. XRD patterns were acquired using a Bruker D8 Advance diffractometer with Cu Kα radiation (λ = 1.5405 Å). The surface area and pore size distribution were determined using an ASAP 2020 surface area analyzer from Micromeritics Co., USA. Structural dimensions at the nanoscale from SAXS were analyzed using a Bruker Nanostar. Surface morphology was examined via FESEM using a Hitachi SU 5000 microscope at an accelerating voltage of 20 kV. HRTEM was conducted using a JEOL JEM-F200, equipped with a JED-2300T energy dispersive spectrometer. XPS spectra was analyzed using a Thermo Scientific K-Alpha instrument with an Al Kα X-ray source (hv = 1486.6 eV).

In-situ mechanical tests

In-situ tensile tests were conducted using a Picoindenter 85 nanoindenter (Pi-85) integrated within a Quanta 250 FEG SEM, coupled with a PTP device. Individual CNFs were fixed onto the PTP sample area via FIB techniques[9,29,41]. Their average diameters and initial lengths were measured based on SEM observations. The cross-sectional area of each cylindrical CNF was calculated with its diameter, while the initial length was defined as the distance between two fixed points. These measurements were essential for the quantitative analysis of mechanical properties. Prior to testing, a conductive diamond flat punch with a diameter of 20 μm was calibrated. The flat probe was then positioned to contact the semicircular end of the CNF mounted on the PTP device. Tensile testing was performed in displacement control mode at a rate of 5 nm s^{-1} until fracture occurred. Force and displacement data were dynamically recorded and and concurrently captured via real-time movie. The resulting force-displacement curve contained contributions from both the PTP device and the CNF sample. Thus, the inherent contribution of the PTP device was subtracted to determine the force applied to the CNF sample. Bending tests were carried out using a Thermo Scientific Helios 5 UX FIB-SEM.

MD simulations

The MD simulations were performed using LAMMPS[71], with the Matsui-Akaogi force field employed (LAMMPS, version 23 Jun 2022)[33–35]. This force field accounts for two key contributions: (i) electrostatic interactions and (ii) van der Waals interactions, expressed in the Buckingham potential form[33]. The interaction energy U between atoms i and j is

given by:

$$U = A_{ij} \exp\left(-\frac{r_{ij}}{\rho_{ij}}\right) - \frac{C_{ij}}{r_{ij}^6} + \frac{q_i q_i}{r_{ij}} \tag{4}$$

Here, r_{ij} denotes the interatomic distance, and q_{ij} represents the critical shielding length, while A_{ij} and C_{ij} are the strength parameters for repulsive and attractive dipole-dipole interactions, respectively[34]. For electrostatic interactions, this force field assigns partial charges of +2.196 for Ti and −1.098 for O. The Buckingham potential incorporates contributions from the Born-Mayer repulsion potential and dipole-dipole interactions. The DP TiO_2 models were constructed with dimensions of 12.32 nm × 12.32 nm × 11.84 nm, embedding eight nanocrystals, each with a radius of 1.75 nm. Distinct configurations of DP models were created based on the nanograin distribution: uniform and aggregated arrangements. Following energy minimization, the structures were optimized using two NVT ensembles at 300 K and 3300 K, regulated by a Nose-Hoover thermostat. To ensure accuracy and reproducibility, timesteps of 1.0 fs and 0.5 fs were both tested during the simulations. The NVT optimization process was conducted for 100 ps to achieve stable structures. Subsequently, uniaxial tensile simulations were performed by extending the simulation box along the x-axis at a strain rate of $1 \times 10^9 \, s^{-1}$ to examine the mechanical behavior[6,27,36,37]. Atomic motions were calculated using the Velocity-Verlet algorithm.

Reporting summary

Further information on research design is available in the Nature Portfolio Reporting Summary linked to this article.

Data availability

The data generated in this study are provided in the Source Data file. Source data are provided with this paper.

References

1. Bouville, F. et al. Strong, tough and stiff bioinspired ceramics from brittle constituents. *Nat. Mater.* **13**, 508 (2014).
2. Liu, G. et al. 4D Additive-subtractive manufacturing of shape memory ceramics. *Adv. Mater.* **35**, 2302108 (2023).
3. Zhang, J. et al. Plastic deformation in silicon nitride ceramics via bond switching at coherent interfaces. *Science* **378**, 371 (2022).
4. Guo, J. et al. Hypocrystalline ceramic aerogels for thermal insulation at extreme conditions. *Nature* **606**, 909 (2022).
5. Xue, J., Wu, T., Dai, Y. & Xia, Y. Electrospinning and electrospun nanofibers: methods, materials, and applications. *Chem. Rev.* **119**, 5298 (2019).
6. Li, L. et al. Nanograin-glass dual-phasic, elasto-flexible, fatigue-tolerant, and heat-insulating ceramic sponges at large scales. *Mater. Today* **54**, 72 (2022).
7. Zhang, Y. et al. Superior flexibility in oxide ceramic crystal nanofibers. *Adv. Mater.* **33**, 2105011 (2021).
8. Jia, C. et al. Highly compressible and anisotropic lamellar ceramic sponges with superior thermal insulation and acoustic absorption performances. *Nat. Commun.* **11**, 3732 (2020).
9. Cheng, X. et al. Way to a library of Ti-series oxide nanofiber sponges that are highly stretchable, compressible, and bendable. *Adv. Mater.* **36**, 2307690 (2024).
10. Liu, M. et al. Composite superelastic aerogel scaffolds containing flexible SiO_2 nanofibers promote bone regeneration. *Adv. Healthc. Mater.* **11**, 2200499 (2022).
11. Wang, B. et al. Flexible and stretchable metal oxide nanofiber networks for multimodal and monolithically integrated wearable electronics. *Nat. Commun.* **11**, 2405 (2020).
12. Wu, F. et al. The rising of flexible and elastic ceramic fiber materials: fundamental concept, design principle, and toughening mechanism. *Adv. Funct. Mater.* **32**, 2207130 (2022).
13. Ren, B. et al. Nanofibrous aerogel bulk assembled by cross-linked SiC/SiO_x core-shell nanofibers with multifunctionality and temperature-invariant hyperelasticity. *ACS Nano* **13**, 11603 (2019).
14. Zhou, Y. et al. Highly efficient thermo-acoustic insulating aerogels enabled by resonant cavity engineering. *ACS Nano* **17**, 14883 (2023).
15. Cheng, X., Liu, Y.-T., Si, Y., Yu, J. & Ding, B. Direct synthesis of highly stretchable ceramic nanofibrous aerogels via 3D reaction electrospinning. *Nat. Commun.* **13**, 2637 (2022).
16. Wu, H., Pan, W., Lin, D. & Li, H. Electrospinning of ceramic nanofibers: fabrication, assembly and applications. *J. Adv. Ceram.* **1**, 2 (2012).
17. Liao, X. et al. High strength in combination with high toughness in robust and sustainable polymeric materials. *Science* **366**, 1376 (2019).
18. Oh, M. H. et al. Design and synthesis of multigrain nanocrystals via geometric misfit strain. *Nature* **577**, 359 (2020).
19. Fan, G. J., Choo, H., Liaw, P. K. & Lavernia, E. J. A model for the inverse Hall-Petch relation of nanocrystalline materials. *Mater. Sci. Eng. A* **409**, 243 (2005).
20. Zhao, H. et al. Multiscale engineered artificial tooth enamel. *Science* **375**, 551 (2022).
21. Gellen, T. A., Lem, J. & Turner, D. B. Probing homogeneous line broadening in CdSe nanocrystals using multidimensional electronic spectroscopy. *Nano Lett.* **17**, 2809 (2017).
22. Li, J. et al. Nanoscale stacking fault-assisted room temperature plasticity in flash-sintered TiO_2. *Sci. Adv.* **5**, eaaw5519 (2019).
23. Shen, C. et al. Achieving room temperature plasticity in brittle ceramics through elevated temperature preloading. *Sci. Adv.* **10**, eadj4079 (2024).
24. Ming, K. et al. Enhancing strength and ductility via crystalline-amorphous nanoarchitectures in TiZr-based alloys. *Sci. Adv.* **8**, eabm2884 (2022).
25. Wu, Y., Tong, K., Zhao, Z. & Tian, Y. Strengthening and toughening by constructing crystalline-amorphous nanoarchitecture. *Matter* **6**, 7 (2023).
26. Li, F. et al. Dual-phase super-strong and elastic ceramic. *ACS Nano* **13**, 4191 (2019).
27. Zhao, Y. et al. Dual phase nano-particulate AlN composite - a kind of ceramics with high strength and ductility. *Ceram. Int.* **45**, 19845 (2019).
28. Fu, X. et al. The innate interfacial elastic strain field of a transformable B2 precipitate embedded in an amorphous matrix. *Npj Comput. Mater.* **9**, 226 (2023).
29. Liu, C. et al. High toughness combined with high strength in oxide ceramic nanofibers. *Adv. Mater.* **35**, 2304401 (2023).
30. Wang, Z. et al. High-quality semiconductor fibres via mechanical design. *Nature* **626**, 72 (2024).
31. Hwang, T.-K., Hong, C.-S. & Kim, C.-G. Size effect on the fiber strength of composite pressure vessels. *Compos. Struct.* **59**, 489 (2003).
32. Zok, F. W. On weakest link theory and Weibull statistics. *J. Am. Ceram. Soc.* **100**, 1265 (2017).
33. Luan, B., Huynh, T. & Zhou, R. Simplified TiO_2 force fields for studies of its interaction with biomolecules. *J. Chem. Phys.* **142**, 234102 (2015).
34. Zhang, S. & Wu, Y. Investigating the crystallization behavior of TiO_2 during annealing: molecular dynamics simulations. *AIP Adv.* **13**, 085226 (2023).
35. Koparde, V. N. & Cummings, P. T. Molecular dynamics study of water adsorption on TiO_2 nanoparticles. *J. Phys. Chem. C.* **111**, 6920 (2007).

36. Weng, S. et al. Molecular dynamics study of strengthening mechanism of nanolaminated graphene/Cu composites under compression. *Sci. Rep.* **8**, 3089 (2018).

37. Pan, A. et al. Molecular dynamics simulation of the orientation and temperature dependence in $MgAl_2O_4$ spinel. *J. Mater. Sci.* **59**, 12526 (2024).

38. Luo, H., Zhang, H., Sheng, H., Liu, J. P. & Szlufarska, I. Amorphous shear bands in $SmCo_5$. *Mater. Sci. Eng. A* **785**, 139340 (2020).

39. Reddy, K. M., Liu, P., Hirata, A., Fujita, T. & Chen, M. W. Atomic structure of amorphous shear bands in boron carbide. *Nat. Commun.* **4**, 2483 (2013).

40. An, Q. et al. Nucleation of amorphous shear bands at nanotwins in boron suboxide. *Nat. Commun.* **7**, 11001 (2016).

41. Xu, Z. et al. Inhibited grain growth through phase transition modulation enables excellent mechanical properties in oxide ceramic nanofibers up to 1700 °C. *Adv. Mater.* **35**, 2305336 (2023).

42. Hench, L. L. & West, J. K. The sol-gel process. *Chem. Rev.* **90**, 33 (1990).

43. Hector, A. L. Materials synthesis using oxide free sol-gel systems. *Chem. Soc. Rev.* **36**, 1745 (2007).

44. Danks, A. E., Hall, S. R. & Schnepp, Z. The evolution of 'sol-gel' chemistry as a technique for materials synthesis. *Mater. Horiz.* **3**, 91 (2016).

45. Kemnitz, E. & Noack, J. The non-aqueous fluorolytic sol-gel synthesis of nanoscaled metal fluorides. *Dalton Trans.* **44**, 19411 (2015).

46. Podsiadlo, P. et al. The role of order, nanocrystal size, and capping ligands in the collective mechanical response of three-dimensional nanocrystal solids. *J. Am. Chem. Soc.* **132**, 8953 (2010).

47. Doeuff, S., Henry, M., Sanchez, C. & Livage, J. Hydrolysis of titanium alkoxides: modification of the molecular precursor by acetic acid. *J. Non-Cryst. Solids* **89**, 206 (1987).

48. Czakler, M., Artner, C. & Schubert, U. Preparation of carboxylato-coordinated titanium alkoxides from carboxylic anhydrides: alkoxido group transfer from metal atom to carbonyl group. *Eur. J. Inorg. Chem.* **2012**, 3485 (2012).

49. Pope, E. J. A. & Mackenzie, J. D. Theoretical modelling of the structural evolution of gels. *J. Non-Cryst. Solids* **101**, 198 (1988).

50. Brasseur, A. et al. Rheological characterization of $BaTiO_3$ sol-gel transition. *J. Sol.-Gel Sci. Technol.* **9**, 5 (1997).

51. Marx, N., Ponjavic, A., Taylor, R. I. & Spikes, H. A. Study of permanent shear thinning of VM polymer solutions. *Tribol. Lett.* **65**, 106 (2017).

52. Utracki, L. A. & Simha, R. Viscosity of polymer solutions: scaling relationships. *J. Rheol.* **25**, 329 (1981).

53. Breki, A. & Nosonovsky, M. Einstein's viscosity equation for nano-lubricated friction. *Langmuir* **34**, 12968 (2018).

54. Jeon, S. et al. Reversible disorder-order transitions in atomic crystal nucleation. *Science* **371**, 498 (2021).

55. Wang, T. et al. In situ observation of nucleation and crystallization of a single nanoparticle in transparent media. *J. Phys. Chem. C.* **124**, 15533 (2020).

56. Zhang, Z. et al. Multistep nucleation visualized during solid-state crystallization. *Mater. Horiz.* **9**, 1670 (2022).

57. Zhang, S. et al. Ambient-conditions spinning of functional soft fibers via engineering molecular chain networks and phase separation. *Nat. Commun.* **14**, 3245 (2023).

58. Albetran, H., O'Connor, B. H. & Low, I. M. Activation energies for phase transformations in electrospun titania nanofibers: comparing the influence of argon and air atmospheres. *Appl. Phys. A* **122**, 367 (2016).

59. Li, J. & Deepak, F. L. In situ kinetic observations on crystal nucleation and growth. *Chem. Rev.* **122**, 16911 (2022).

60. Yang, J. et al. Amorphous-phase-mediated crystallization of Ni nanocrystals revealed by high-resolution liquid-phase electron microscopy. *J. Am. Chem. Soc.* **141**, 763 (2019).

61. Ambroz, F., Macdonald, T. J., Martis, V. & Parkin, I. P. Evaluation of the BET Theory for the characterization of meso and microporous MOFs. *Small Methods* **2**, 1800173 (2018).

62. Shimizu, S. & Matubayasi, N. Surface area estimation: replacing the Brunauer-Emmett-Teller model with the statistical thermodynamic fluctuation theory. *Langmuir* **38**, 7989 (2022).

63. Shimizu, S. & Matubayasi, N. Understanding sorption mechanisms directly from isotherms. *Langmuir* **39**, 6113 (2023).

64. Lin, S. et al. Triboelectric micro-flexure-sensitive fiber electronics. *Nat. Commun.* **15**, 2374 (2024).

65. Li, Y. et al. Theoretical insights into the Peierls plasticity in $SrTiO_3$ ceramics via dislocation remodelling. *Nat. Commun.* **13**, 6925 (2022).

66. Yao, S.-W., Li, C.-J., Tian, J.-J., Yang, G.-J. & Li, C.-X. Conditions and mechanisms for the bonding of a molten ceramic droplet to a substrate after high-speed impact. *Acta Mater.* **119**, 9 (2016).

67. Kubo, T., Orita, H. & Nozoye, H. Surface structures of rutile TiO_2 (011). *J. Am. Chem. Soc.* **129**, 10474 (2007).

68. Zheng, K. et al. Electron-beam-assisted superplastic shaping of nanoscale amorphous silica. *Nat. Commun.* **1**, 24 (2010).

69. Frankberg, E. J. et al. Highly ductile amorphous oxide at room temperature and high strain rate. *Science* **366**, 864 (2019).

70. Pietrak, K. & Wiśniewski, T. S. A review of models for effective thermal conductivity of composite materials. *J. Power Technol.* **95**, 14 (2015).

71. Plimpton S. Fast parallel algorithms for short-range molecular dynamics. *J. Comput. Phys.* **117**, 1 (1995).

Acknowledgements

Author contributions

S.Q., S.Z., S.L., and J.D. conducted the experimental studies. S.Q., F.W. and H.L. carried out the analysis. S.Q. and X.Z. performed the computational studies. B.D., Y.L. and J.Y. supervised the work.

Competing interests

The authors declare no competing interests.

Additional information